

Banner appropriate to article type will appear here in typeset article

# Learning rheological parameters of non-Newtonian fluids from velocimetry data

Alexandros Kontogiannis<sup>1†</sup>, Richard Hodgkinson<sup>2</sup> and Emily L. Manchester<sup>3</sup>

<sup>1</sup>Engineering Department, University of Cambridge, Trumpington Street, Cambridge, CB2 1PZ, UK

<sup>2</sup>Materials Science and Engineering Department, University of Sheffield, Sheffield, S1 3JD, UK

<sup>3</sup>Mechanical & Aerospace Engineering Department, University of Manchester, Manchester, M13 9PL, UK

(Received xx; revised xx; accepted xx)

We solve a Bayesian inverse Navier–Stokes (N–S) problem that assimilates velocimetry data in order to jointly reconstruct the flow field and learn the unknown N–S parameters. By incorporating a Carreau shear-thinning viscosity model into the N–S problem, we devise an algorithm that learns the most likely Carreau parameters of a shear-thinning fluid, and estimates their uncertainties, from velocimetry data alone. We then conduct a flow-MRI experiment to obtain velocimetry data of an axisymmetric laminar jet through an idealised medical device (FDA nozzle) for a blood analogue fluid. We show that the algorithm can successfully reconstruct the flow field by learning the most likely Carreau parameters, and that the learned parameters are in very good agreement with rheometry measurements. The algorithm accepts any algebraic effective viscosity model, as long as the model is differentiable, and it can be extended to more complicated non-Newtonian fluids (e.g. Oldroyd-B fluid) if a viscoelastic model is incorporated into the N–S problem.

**Key words:** rheology, Bayesian inference, magnetic resonance velocimetry

## 1. Introduction

Magnetic resonance velocimetry (flow-MRI) is an experimental technique used to measure fluid velocities in time and three-dimensional space. Flow-MRI is most commonly known for its use *in vivo* in clinical settings, however, it is gaining popularity within the wider scientific community for *in vitro* applications (Elkins & Alley 2007). Whilst flow-MRI can provide reliable velocity measurements, it does not provide information on fluid properties such as rheology or pressure, which require additional experiments. Various experimental approaches are capable of measuring a fluid’s shear stress-strain curve. Acquiring this non-invasively is challenging as it requires knowledge about both the stress and strain, and some degree of control of either. Common experimental techniques to measure fluid viscosity include rotational and capillary rheometry, which involve passing a fluid sample through a precision geometry and measuring shear-rate, torque, or pressure drop. Other techniques

† Email address for correspondence: ak2239@cam.ac.uk

are available such as industrial ‘in-line’ and ‘on-line’ rheometry, or ultrasound velocity profiling. However, these methods are either highly invasive (Magalhães *et al.* 2017) or require pressure drop measurements (K. *et al.* 2022). Due to the additional costs and complexities associated with rheometry experiments, it is not always feasible to acquire rheological data. For computational fluid dynamic (CFD) simulations of non-Newtonian fluids, rheological behaviours are captured in mathematical models via adjustable parameters. If unknown, model parameters are typically selected using values taken from the literature. One such application is the field of biomedical engineering, where flow-MRI data is commonly used to inform patient-specific cardiovascular models. Without patient specific blood rheology, CFD models lack accuracy. Ranftl *et al.* (2023) performed an uncertainty quantification study to investigate the impact of non-Newtonian and Newtonian CFD models on haemodynamic outputs. They found that specifying patient rheological properties is necessary for accurate wall shear stress predictions. This is especially important in diseases where blood properties differ from healthy populations and in small arteries where non-Newtonian effects dominate.

Bayesian inference is a data-driven technique that can be used to estimate unknown physical or model parameters and their uncertainties from experimental reference data. Worthen *et al.* (2014) used such an approach to infer two unknown parameters of a constitutive equation for viscosity in mantle flow. The forward problem was governed by a Nonlinear Stokes problem and experimental reference data took the form of surface velocity measurements. Their method was able to recover constant and spatially-varying parameters reasonably well. Although Worthen’s problem differs from ours, the underlying approach is similar and effectively demonstrates the feasibility of inferring rheological parameters from experimental measurements.

In this study we aim to infer the rheological parameters of a shear-thinning blood analogue from flow-MRI-measured *velocity fields* alone. The Carreau model is selected to represent the non-Newtonian fluid behaviour (Sequeira & Janela 2007) because it is differentiable and bounded. Fluid experiments are performed using an idealised medical device, namely the Food and Drug Administration’s (FDA) benchmark nozzle model, and data is assimilated using a Bayesian inverse Navier–Stokes problem that jointly reconstructs the flow field and learns the Carreau parameters. To the best of the authors’ knowledge, this is the first time flow-MRI has been used for a non-invasive measurement of rheological parameters without a pressure drop measurement.

## 2. Bayesian inversion of the Navier–Stokes problem

We learn the rheology of a non-Newtonian fluid from velocimetry data by solving a *Bayesian inverse N–S problem*. We first assume that there is a N–S problem with a Carreau fluid model, which can explain the velocimetry data,  $\mathbf{u}^\star$ . That is, there exist N–S parameters  $\mathbf{x}^\circ$  such that

$$\mathbf{u}^\star - \mathcal{Z}\mathbf{x}^\circ = \boldsymbol{\varepsilon} \sim \mathcal{N}(\mathbf{0}, \mathbf{C}_{\mathbf{u}^\star}) \quad , \quad (2.1)$$

where  $\mathcal{Z}$  is the nonlinear operator that maps N–S parameters to N–S solutions projected into the data space, and  $\boldsymbol{\varepsilon}$  is Gaussian noise with zero mean and covariance operator  $\mathbf{C}_{\mathbf{u}^\star}$ . We do not know  $\mathbf{x}^\circ$ , but we assume that its prior probability distribution is  $\mathcal{N}(\bar{\mathbf{x}}, \mathbf{C}_{\bar{\mathbf{x}}})$ , where  $\bar{\mathbf{x}}$  is the prior mean, and  $\mathbf{C}_{\bar{\mathbf{x}}}$  is the prior covariance operator. Using Bayes’ theorem we then find that the posterior probability density function (p.d.f.) of  $\mathbf{x}$ , given the data  $\mathbf{u}^\star$ , is given by

$$\pi(\mathbf{x}|\mathbf{u}^\star) \propto \pi(\mathbf{u}^\star|\mathbf{x}) \pi(\mathbf{x}) = \exp\left(-\frac{1}{2}\|\mathbf{u}^\star - \mathcal{Z}\mathbf{x}\|_{\mathbf{C}_{\mathbf{u}^\star}}^2 - \frac{1}{2}\|\mathbf{x} - \bar{\mathbf{x}}\|_{\mathbf{C}_{\bar{\mathbf{x}}}}^2\right) \quad , \quad (2.2)$$

where  $\pi(\mathbf{u}^\star|\mathbf{x})$  is the data likelihood,  $\pi(\mathbf{x})$  is the prior p.d.f. of  $\mathbf{x}$ , and  $\|\cdot, \cdot\|_{\mathbf{C}}^2 := \langle \cdot, \mathbf{C}^{-1} \cdot \rangle$  is the covariance-weighted  $L^2$ -norm. The most likely parameters,  $\mathbf{x}^\circ$ , in the sense that they

maximise the posterior p.d.f. (maximum *a posteriori* probability, or MAP estimator), are given implicitly as the solution of the nonlinear optimisation problem

$$\mathbf{x}^\circ \equiv \underset{\mathbf{x}}{\operatorname{argmin}} \mathcal{J} \quad , \quad \text{where} \quad \mathcal{J} := -\log \pi(\mathbf{x}|\mathbf{u}^\star) \quad . \quad (2.3)$$

Using a first order Taylor expansion of  $\mathcal{Z}$  around  $\mathbf{x}_k$ , given by

$$\mathcal{Z}\mathbf{x} \simeq \mathcal{Z}\mathbf{x}_k + \mathcal{G}_k(\mathbf{x} - \mathbf{x}_k) \quad , \quad (2.4)$$

the optimality conditions of problem (2.3) lead to the following iteration (Tarantola 2005)

$$\mathbf{x}_{k+1} \leftarrow \mathbf{x}_k + \tau_k C_{\mathbf{x}_k} (D_{\mathbf{x}} \mathcal{J})_k \quad , \quad (2.5)$$

where  $(D_{\mathbf{x}} \mathcal{J})_k := \mathcal{G}_k^* C_{\mathbf{u}^\star}^{-1}(\mathbf{u}^\star - \mathcal{Z}\mathbf{x}_k) + C_{\bar{\mathbf{x}}}^{-1}(\mathbf{x}_k - \bar{\mathbf{x}})$ ,  $\tau_k$  is the step size at iteration  $k$ , which is determined by a line-search algorithm,  $\mathcal{G}_k^*$  is the adjoint of  $\mathcal{G}_k$ , and  $C_{\mathbf{x}_k}$  is the posterior covariance operator at iteration  $k$ , which is given by

$$C_{\mathbf{x}_k} := (\mathcal{G}_k^* C_{\mathbf{u}^\star}^{-1} \mathcal{G}_k + C_{\bar{\mathbf{x}}}^{-1})^{-1} \quad . \quad (2.6)$$

The posterior covariance operator around the MAP estimate,  $C_{\mathbf{x}^\circ}$ , can then be used to approximate the posterior p.d.f. such that

$$\pi(\mathbf{x}|\mathbf{u}^\star) \simeq \exp\left(-\frac{1}{2}\|\mathbf{x} - \mathbf{x}^\circ\|_{C_{\mathbf{x}^\circ}}^2 - \text{const.}\right) \quad , \quad (2.7)$$

which is known as the *Laplace approximation*. For linear models, the approximation is exact when both  $\pi(\mathbf{u}^\star|\mathbf{x})$  and  $\pi(\mathbf{x})$  are normal. For nonlinear models, the accuracy of the approximation depends on the behaviour of the operator  $\mathcal{Z}$  around the critical point  $\mathbf{x}^\circ$ .

### 2.1. N-S problem and the operators $\mathcal{Z}$ , $\mathcal{G}$

In order to solve the inverse problem (2.3) using formulas (2.5), (2.6), we need to define  $\mathcal{Z}$  and  $\mathcal{G}$ . To that end, we start from the N-S boundary value problem in  $\Omega \subset \mathbb{R}^3$

$$\begin{aligned} \mathbf{u} \cdot \nabla \mathbf{u} - \nabla \cdot (2\nu_e \nabla^s \mathbf{u}) + \nabla p &= \mathbf{0} \quad \text{and} \quad \nabla \cdot \mathbf{u} = 0 \quad \text{in} \quad \Omega \quad , \\ \mathbf{u} &= \mathbf{0} \quad \text{on} \quad \Gamma \quad , \quad \mathbf{u} = \mathbf{g}_i \quad \text{on} \quad \Gamma_i \quad , \quad -2\nu_e \nabla^s \mathbf{u} \cdot \mathbf{v} + p\mathbf{v} = \mathbf{g}_o \quad \text{on} \quad \Gamma_o \quad , \end{aligned} \quad (2.8)$$

where  $\mathbf{u}$  is the velocity,  $p \leftarrow p/\rho$  is the reduced pressure,  $\rho$  is the density,  $\nu_e$  is the *effective* (kinematic) viscosity,  $(\nabla^s \mathbf{u})_{ij} := \frac{1}{2}(\partial_j u_i + \partial_i u_j)$  is the strain-rate tensor,  $\mathbf{g}_i$  is the Dirichlet boundary condition (b.c.) at the inlet  $\Gamma_i$ ,  $\mathbf{g}_o$  is the natural b.c. at the outlet  $\Gamma_o$ , and  $\mathbf{v}$  is the unit normal vector on the boundary  $\partial\Omega = \Gamma \cup \Gamma_i \cup \Gamma_o$ , where  $\Gamma$  is the no-slip boundary (wall). The construction of the operators  $\mathcal{Z}$ ,  $\mathcal{G}$  of the generalised inverse N-S problem, whose unknown parameters are the shape of the domain  $\Omega$ , the boundary conditions  $\mathbf{g}_i$ ,  $\mathbf{g}_o$ , and the viscosity field  $\nu_e$ , is treated in Kontogiannis *et al.* (2022, 2024). Here, we fix the geometry,  $\Omega$ , and the outlet b.c.,  $\mathbf{g}_o$ , and infer only the inlet b.c.,  $\mathbf{g}_i$ , and the effective viscosity field,  $\nu_e$ . We further introduce the Carreau model for the effective viscosity field, which is given by

$$\mu_e(\dot{\gamma}; \mathbf{p}_\mu) := \mu_\infty + \delta\mu(1 + (\lambda\dot{\gamma})^2)^{(n-1)/2} \quad , \quad (2.9)$$

where  $\mu_e := \nu_e \rho$ ,  $\dot{\gamma}(\mathbf{u}) := \sqrt{2\nabla^s \mathbf{u} : \nabla^s \mathbf{u}}$  is the magnitude of the strain-rate tensor, and  $\mathbf{p}_\mu := (\mu_\infty, \delta\mu, \lambda, n)$  are the Carreau fluid parameters. In order to infer the most likely viscosity field,  $\mu_e^\circ$ , we therefore need to infer the most likely Carreau fluid parameters,  $\mathbf{p}_\mu^\circ$ .

After linearising problem (2.8) around  $\mathbf{u}_k$ , we obtain  $\mathbf{u}(\mathbf{x}) \simeq \mathbf{u}_k + \mathcal{A}_k(\mathbf{x} - \mathbf{x}_k)$ , where  $\mathcal{A}_k \equiv ((D_{\mathbf{u}}^\mathcal{M})^{-1} D_{\mathbf{x}}^\mathcal{M})_k$ , with  $\mathcal{A}_k$  being a linear, *invertible* operator, which encapsulates the inverse Jacobian of the N-S problem,  $(D_{\mathbf{u}}^\mathcal{M})^{-1}$ , and the generalised gradient of the velocity field with respect to the parameters  $\mathbf{x}$ ,  $D_{\mathbf{x}}^\mathcal{M}$ . Observing that  $\mathcal{Z}$ ,  $\mathcal{G}$  map from the N-S

parameter space to the (velocimetry) data space, we define  $\mathcal{Z} := S\mathcal{Q}$ , and  $\mathcal{G}_k := S\mathcal{A}_k$ , where  $S : \mathbf{M} \rightarrow \mathbf{D}$  is a projection from the model space,  $\mathbf{M}$ , to the data space,  $\mathbf{D}$ , and  $\mathcal{Q}$  is the operator that maps  $\mathbf{x}$  to  $\mathbf{u}$ , i.e. solves the N-S problem. (Operators  $S, \mathcal{Q}, \mathcal{A}$  are derived in Kontogiannis *et al.* (2024) from the weak form of the N-S problem (2.8),  $\mathcal{M}$ .) Based on the above definitions, and due to (2.5), we observe that the *model contribution* to the objective's steepest descent direction, for the Carreau parameters,  $\mathbf{p}_\mu$ , is

$$\delta \mathbf{p}_\mu := \mathcal{G}_k^* C_{\mathbf{u}^\star}^{-1} (\mathbf{u}^\star - \mathcal{Z} \mathbf{x}_k) = \underbrace{(D_{\mathbf{p}_\mu}^{\mathcal{M}})^* ((D_{\mathbf{u}}^{\mathcal{M}})^*)^{-1}}_{D_{\mathbf{u}}^{\mathbf{p}_\mu}} \underbrace{S^* C_{\mathbf{u}^\star}^{-1} (\mathbf{u}^\star - S \mathbf{u}_k)}_{\text{model-data discrepancy } \delta \mathbf{u} \in \mathbf{M}} . \quad (2.10)$$

Even though  $D_{\mathbf{u}}^{\mathcal{M}}$  is invertible, for large-scale problems, such as those in fluid dynamics, its inverse,  $(D_{\mathbf{u}}^{\mathcal{M}})^{-1}$ , cannot be stored in computer memory because its discrete form produces a dense matrix. The discrete form of  $D_{\mathbf{u}}^{\mathcal{M}}$ , however, produces a sparse matrix. Consequently, instead of using the explicit formula (2.10), the steepest descent directions are given by

$$\delta \mathbf{p}_\mu := (D_{\mathbf{p}_\mu}^{\mathcal{M}})^* \mathbf{v}_k = 2\rho \int_{\Omega} (D_{\mathbf{p}_\mu} \mu_e)_k (\nabla^s \mathbf{u}_k : \nabla^s \mathbf{v}_k) , \quad (2.11)$$

where  $(D_{\mathbf{p}_\mu} \mu_e)_k \equiv D_{\mathbf{p}_\mu} \mu_e (\dot{\gamma}(\mathbf{u}_k); (\mathbf{p}_\mu)_k)$  consists of the derivatives of the Carreau model with respect to its parameters, and  $\mathbf{v}_k$  is the adjoint velocity field, which is obtained by solving the following linear operator equation

$$A \mathbf{v}_k = \mathbf{b} , \quad \text{where } A \equiv (D_{\mathbf{u}}^{\mathcal{M}})^* , \quad \text{and } \mathbf{b} \equiv S^* C_{\mathbf{u}^\star}^{-1} (\mathbf{u}^\star - S \mathbf{u}_k) . \quad (2.12)$$

Instead of explicitly computing  $C_{\mathbf{x}_k}$  at every iteration using formula (2.6), we approximate  $C_{\mathbf{x}_k}$  using the damped BFGS quasi-Newton method (Goldfarb *et al.* 2020), which ensures that  $C_{\mathbf{x}_k}$  remains positive definite, and its approximation remains numerically stable.

---

**Algorithm 1:** Learning rheological parameters from velocimetry data

---

**Input:** velocimetry data,  $\mathbf{u}^\star$ , data cov.,  $C_{\mathbf{u}^\star}$ , prior mean,  $\bar{\mathbf{x}}$ , and prior cov.  $C_{\bar{\mathbf{x}}}$   
**Initialisation:** set  $k \leftarrow 0$ ,  $\mathbf{x}_0 \leftarrow \bar{\mathbf{x}}$ , and compute initial velocity field  $\mathbf{u}_0 \leftarrow \mathcal{Q} \mathbf{x}_0$   
**while** termination\_criterion\_is\_not\_met **do**  
     $(\mathbf{v}, q)_k \leftarrow$  solve adjoint N-S problem around  $\mathbf{u}_k$  (eq. (2.12))  
     $(D_{\mathbf{x}} \mathcal{F})_k \leftarrow$  compute steepest descent direction (eq. (2.5), (2.11))  
     $C_{\mathbf{x}_k}, \tau_k \leftarrow$  update post. cov. approx. and find step size (damped BFGS)  
     $\mathbf{x}_{k+1} \leftarrow \mathbf{x}_k + \tau_k C_{\mathbf{x}_k} D_{\mathbf{x}} \mathcal{F}$ , i.e. update N-S parameters  
     $\mathbf{u}_{k+1} \leftarrow \mathcal{Q} \mathbf{x}_{k+1}$ , i.e. update N-S solution, and set  $k \leftarrow k + 1$   
**Output:** MAP estimates:  $\mathbf{u}^\circ \leftarrow \mathbf{u}_k$ ,  $p^\circ \leftarrow p_k$ ,  $\mathbf{x}^\circ \leftarrow \mathbf{x}_k$  and post. covariance  $C_{\mathbf{x}^\circ}$

---

### 3. Flow-MRI experiment of a non-Newtonian laminar jet

The test section is part of the FDA nozzle (Hariharan *et al.* 2011; Stewart *et al.* 2012), which is an axisymmetric pipe that converges to a narrow throat section, followed by a sudden expansion, where a non-Newtonian laminar jet forms (see figure 1). The geometry was 3D-resin-printed to a nominal tolerance of  $\pm 0.2\text{mm}$ . Acrylic tubes were attached upstream and downstream of the test section, and the former was equipped with a flow straightener array. The test section was placed inside a water-filled acrylic outer tube in order to avoid air-induced magnetic susceptibility gradients. A pipe loop provided flow from pumping hardware outside the MRI scanner room, with the return pipe looping back through an annular gap between the

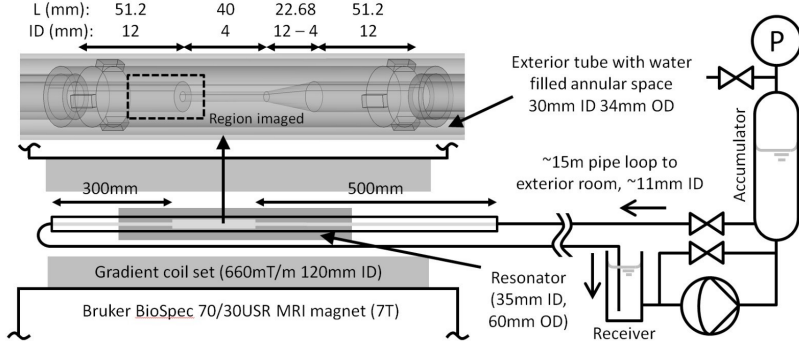


Figure 1: Overall flow system and setup around the MRI scanner with detail of the FDA flow nozzle geometry implemented. ID: Inner diameter, OD: outer diameter.

resonator body and the gradient coil inner diameter. Flow was collected in a receiver reservoir, pumped via a variable speed diaphragm pump, fed to a pulsation dampening accumulator, and then back to the test section. Controlled pump bypass enabled very low flow rates whilst keeping the pump oscillation frequency high. Loop circulation timescales are on the order of the scanning timescale. The flow loop was purged of bubbles after filling, and K-Type and alcohol thermometers measurements indicated a fluid (ambient) temperature of 21.8°C. The test solution used here is a 46wt% haematocrit level blood analogue (Brookshier & Tarbell 1993) (0.5wt% NaCl was omitted because it would interfere with MRI). A 40wt% glycerine solution in deionised water was first prepared and then used as the solvent for a 0.04wt% xanthan gum solution. The solution appears weakly viscoelastic, with viscous stresses above elastic stresses in their 2Hz oscillatory shear tests, justifying the generalised Newtonian fluid assumption. Flow-MRI was performed using a Bruker Biospec 70/30USR 7T preclinical scanner (660 mT/m gradients, 35mm ID resonator coil). Images were acquired with uniform radial pixel spacing of 0.1mm and axial slice thickness of 0.08mm. Four scan repetitions were performed in order to reduce noise (~15 minutes total scanning time).

### 3.1. Flow-MRI data pre-processing

We use phase-contrast MRI and Hadamard encoding to measure all three components of a three-dimensional velocity field using a single set of four, fully-sampled  $k$ -space scans,  $\{s\}_{j=1}^4$ . For each scan we compute its respective complex image,  $w_j$ , which is given by

$$w_j := \rho_j e^{i\varphi_j} = \mathcal{F}^{-1} s_j \quad , \quad (3.1)$$

where  $\rho_j$  is the nuclear spin density image,  $\varphi_j$  is the phase image, and  $\mathcal{F}$  is the Fourier transform. The velocity components  $u_i$ , for  $i = 1, \dots, 3$ , are then given by

$$u_i = c_i h_{ij} \varphi_j \quad , \quad h_{ij} = \begin{pmatrix} -1 & 1 & 1 & -1 \\ -1 & 1 & -1 & 1 \\ -1 & -1 & 1 & 1 \end{pmatrix} \quad , \quad j = 1 \dots 4 \quad , \quad (3.2)$$

where repeated indices imply summation, and  $c_i$  is a known constant that depends on the gyromagnetic ratio of hydrogen and the gradient pulse properties. In order to remove any phase shift contributions that are not caused by the flow, we conduct an additional no-flow experiment. That is, we acquire a set of four  $k$ -space scans,  $\{\bar{s}\}_{j=1}^4$ , for the same geometry and field-of-view, but with zero flow (stagnant fluid). We then obtain the no-flow complex images,  $\bar{w}_j$ , using equation (3.1), and compute the corresponding no-flow velocity images

using equation (3.2), such that  $\bar{u}_i = \bar{c}_i h_{ij} \bar{\varphi}_j$ , where  $\bar{c}_i$  is the no-flow constant, which is known. The corrected velocity is then given by  $u_i = c_i \theta(h_{ij} \varphi_j) - \bar{c}_i \theta(h_{ij} \bar{\varphi}_j)$ , where  $\theta(x) = x - 2\pi(\lfloor (x/\pi) - 1 \rfloor / 2) + 1$  is the phase difference unwrapping function, and  $\lfloor \cdot \rfloor$  denotes integer division. To increase the signal-to-noise ratio (SNR) of steady flow images we acquire  $n$  sets (in this study  $n = 4$ ) of  $k$ -space scans, generate their respective velocity images  $\{u_i\}_{k=1}^n$ , and compute the average velocity image  $\sum_{k=1}^n (u_i)_k / n$ . The noise variance in the averaged velocity images then reduces to  $\sigma^2/n$ , where  $\sigma^2$  is the noise variance of each individual velocity image. We straighten and centre the averaged flow-MRI images, and, since the flow is axisymmetric, we mirror-average the images to further increase SNR and enforce mirror-symmetry. We generate a mask for the region of interest by segmenting the mirror-averaged nuclear spin density image, and apply this mask to the velocity images. Because we solve an inverse N-S problem in a 3D discrete space comprised of trilinear finite elements (voxels), the final pre-processing step is to  $L^2$ -project the 2D axisymmetric flow-MRI images,  $(u_r, u_z)$ , to their corresponding 3D flow field,  $\mathbf{u}^\star = (u_x^\star, u_y^\star, u_z^\star)$ . Note that the 3D data that we generate have the same (2D) spatial resolution as the 2D images.

#### 4. Joint flow field reconstruction and Carreau parameter learning

We apply algorithm 1 to the non-Newtonian axisymmetric jet in order to jointly reconstruct the velocity field and learn the rheological parameters of the Carreau fluid. We use the velocimetry data,  $\mathbf{u}^\star$ , and compute the data noise covariance,  $\mathbf{C}_{\mathbf{u}^\star} = \sigma^2 \mathbf{I}$ , where  $\mathbf{I}$  is the identity operator, and  $\sigma = 0.234$  cm/s (Gudbjartsson & Patz 1995) (For reference, the peak jet velocity is  $\sim 24$  cm/s.) We fix the geometry,  $\Omega$ , which is known (section of FDA nozzle), and the outlet b.c. to  $\mathbf{g}_o \equiv \mathbf{0}$ , and we infer the unknown Carreau parameters and the inlet b.c.,  $\mathbf{g}_i$ . To test the robustness of algorithm 1, we assume high uncertainty in the priors by setting the prior mean and covariance of the Carreau parameters to  $\bar{\mathbf{p}}_\mu = (\mu_\infty, \delta\mu, \lambda, n) = (4 \cdot 10^{-3}, 1 \cdot 10^{-1}, 5, 1)$ ,  $\mathbf{C}_{\bar{\mathbf{p}}_\mu} = \text{diag}(0.5 \cdot 10^{-3}, 0.5 \cdot 10^{-1}, 1, 0.5)^2$ , in SI units, and  $\rho = 1099.3$  kg/m<sup>3</sup>. Note that the prior mean corresponds to a Newtonian fluid with viscosity  $\mu_e(\bar{\mathbf{p}}_\mu) \equiv \bar{\mu}_\infty + \delta\bar{\mu} \simeq 0.1$  Pa.s. We set the prior mean of the inlet b.c. to  $\bar{\mathbf{g}}_i = (\mathbf{S}^\star \mathbf{u}^\star)|_{\Gamma_i}$ , i.e. the restriction of the  $\mathbf{S}^\star$ -projected data on  $\Gamma_i$ , and the prior covariance to  $\mathbf{C}_{\bar{\mathbf{g}}_i} = \sigma_{\bar{\mathbf{g}}_i}^2 \mathbf{I}$ , where  $\sigma_{\bar{\mathbf{g}}_i} = 1$  cm/s. We infer the inlet b.c., instead of fixing its value to  $(\mathbf{S}^\star \mathbf{u}^\star)|_{\Gamma_i}$ , in order to compensate for local imaging artefacts and/or measurement biases on (or near)  $\Gamma_i$ .

##### 4.1. Flow field reconstruction

The reconstructed flow field,  $\mathbf{u}^\circ$ , which is generated using algorithm 1, is shown in figure 2 vs. the velocimetry data,  $\mathbf{u}^\star$ . We define the average model-data distance by  $\mathcal{E}(\mathbf{u}_\square) := |\Omega|^{-1} \|\mathbf{u}_\square^\star - \mathbf{S}\mathbf{u}_\square\|_{L^2(\Omega)}$ , where  $|\Omega|$  is the volume of  $\Omega$ , and  $\square$  is a symbol placeholder. For the reconstructed velocity field,  $\mathbf{u}^\circ$ , we then find  $\mathcal{E}(u_x^\circ) = \mathcal{E}(u_y^\circ) = 0.71\sigma$ ,  $\mathcal{E}(u_z^\circ) = 1.40\sigma$ , and compare this to the distance between the initial guess,  $\mathbf{u}^{(0)}$ , and the data  $\mathcal{E}(u_x^{(0)}) = \mathcal{E}(u_y^{(0)}) = 1.39\sigma$ ,  $\mathcal{E}(u_z^{(0)}) = 5.87\sigma$ . The inferred (MAP) vs. prior strain-rate magnitude,  $\dot{\gamma}$ , and effective viscosity field,  $\mu_e(\dot{\gamma})$ , are shown in figure 3. Note that, we initialise algorithm 1 using the prior means, and thus  $\mu_e^{(0)} = \mu_e(\dot{\gamma}(\mathbf{u}_0); \bar{\mathbf{p}}_\mu) \simeq 0.1$  Pa.s.

##### 4.2. Carreau parameter learning

According to the optimisation log (figure 4a), the algorithm learns the unknown N-S parameters in  $\sim 20$  iterations (i.e. the Carreau parameters and the inlet b.c.), but most of the work is done in  $\sim 10$  iterations. Using the Carreau parameters learned at every step,  $k$ , of the optimisation process, we plot the evolution of the posterior p.d.f. of  $\mu_e$

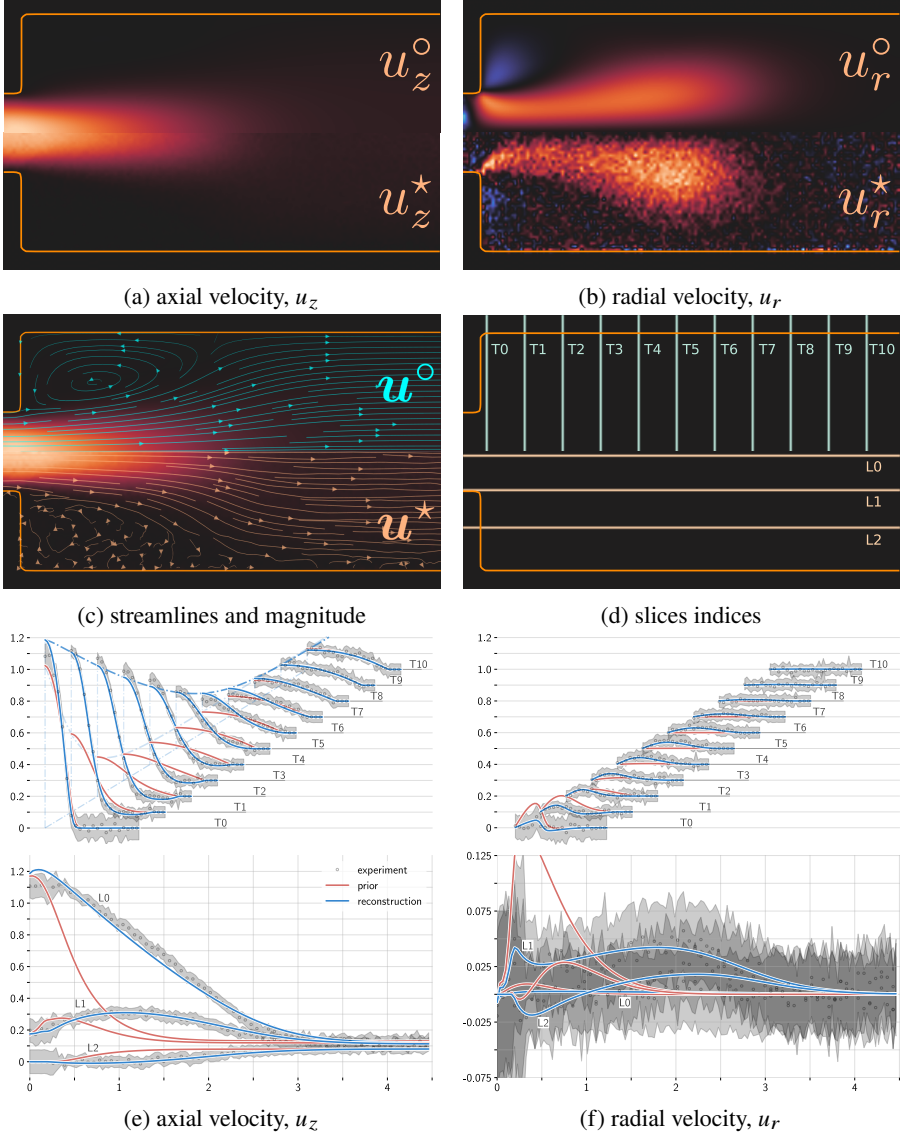


Figure 2: Images and slices of reconstructed (MAP) flow,  $\mathbf{u}^o$ , vs. velocimetry data,  $\mathbf{u}^*$ . In figures 2e and 2f, velocity is normalised by  $U = 20$  cm/s, and length is normalised by  $L = 5$  mm. We separate the transverse slices in the plot by applying a vertical offset of  $0.1n$  to the  $n$ -th slice (the horizontal offset value is immaterial).

(mean,  $\mu_e^{(k)}$ , and covariance,  $C_{\mu_e}^{(k)}$ ) (figure 4b). The posterior covariance of  $\mu_e^{(k)}$  is given by  $C_{\mu_e}^{(k)} := \mathcal{G}_{\mu_e}^{(k)} \tilde{C}_{\mathbf{p}_\mu}^{(k)} (\mathcal{G}_{\mu_e}^{(k)})^*$ , where  $\mathcal{G}_{\mu_e}$  is the Jacobian of the Carreau fluid model (2.9) with respect to its parameters,  $\mathbf{p}_\mu$ , and  $\tilde{C}_{\mathbf{p}_\mu}^{(k)}$  is the BFGS approximation of the posterior covariance of the Carreau parameters,  $C_{\mathbf{p}_\mu}^{(k)}$ . The prior uncertainty, shown in figure 4b as a  $\pm 3\sigma$  red shaded region, is sufficiently high and extends beyond the  $\mu_e - \dot{\gamma}$  plotting range. We observe that the posterior uncertainty of  $\mu_e$  significantly reduces after assimilating the data in the model, and that the highest uncertainty reduction is for  $10 < \dot{\gamma} < 200$ , which is the  $\dot{\gamma}$ -range of the laminar jet (see figure 3a). It is worth mentioning that, even though we observe



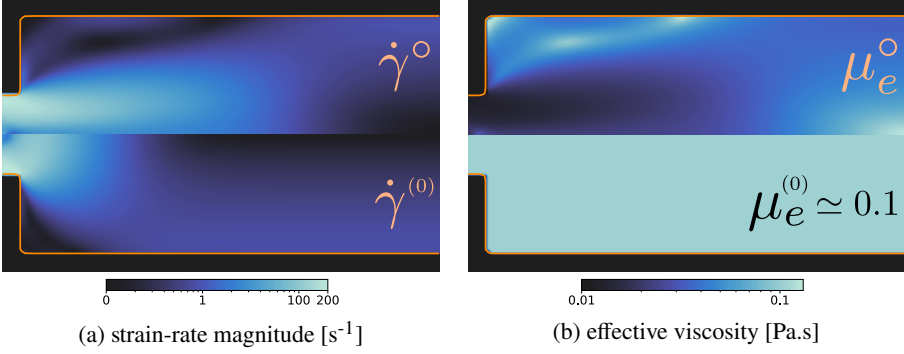


Figure 3: Inferred (MAP) vs. prior strain-rate magnitude,  $\dot{\gamma}$ , and effective viscosity,  $\mu_e$ .

a flow for which  $\dot{\gamma} \in [0, 200]$ , the most informative region is the one around the jet, because i) inertial effects balance viscous effects, and ii) the local velocity-to-noise ratio is high, hence the uncertainty collapse in the jet-operating  $\dot{\gamma}$ -range. The posterior p.d.f evolution of the Carreau parameters is shown in figure 4c. In this case, the prior uncertainty iso-contours can be visualised using hyperellipsoids in  $\mathbb{R}^4$  whose centres are  $\bar{\mathbf{p}}_\mu$ , and axes length proportional to (the columns of)  $C_{\bar{\mathbf{p}}_\mu}$ . To highlight the parameter uncertainty reduction after assimilating the data, we set the origin to  $\bar{\mathbf{p}}_\mu$ , and scale each dimension of  $\mathbb{R}^4$  using (the columns of)  $C_{\bar{\mathbf{p}}_\mu}$ . In this transformed space the prior uncertainty iso-contours are hyperspheres, and the posterior uncertainty iso-contours are hyperellipsoids, whose slices are shown in figure 4c. It is interesting to note that, after assimilating the velocimetry data, the posterior uncertainty collapses along the axes  $n$ ,  $\delta\mu$ , whilst it remains almost unaltered along the axes  $\mu_\infty$ ,  $\lambda$ . This is because, particularly for the asymptotic value  $\mu_\infty (= \mu_e(\dot{\gamma})$  for  $\dot{\gamma} \rightarrow \infty$ ), there is not sufficient information in the data to further collapse the prior uncertainty. To further collapse the uncertainty in the directions  $\mu_\infty, \lambda$ , a new experiment would need to include higher strain-rate magnitudes ( $\dot{\gamma} \gg 200 \text{ s}^{-1}$ ).

#### 4.3. Validation via an independent rheometry experiment

Steady-shear rheometry of the test solution was conducted using a Netzsch Kinexus rheometer with a  $\varnothing 27.5\text{mm}$  cup and a  $\varnothing 25\text{mm}$  bob geometry, at the same temperature as the flow-MRI experiment. The experiment was conducted to validate the Carreau parameters learned from the flow-MRI data (section 4.2) against rheometry data. To find the most likely Carreau parameters that fit the rheometry data, we use Bayesian inversion (see section 2). In this case, operator  $\mathcal{Z}$  corresponds to the Carreau model, given by the explicit relation (2.9), and operator  $\mathcal{G}$  corresponds to the Jacobian of the Carreau model with respect to its parameters. We use the same prior as in section 4. Because the prior uncertainty is sufficiently high relative to the noise variance, the bias it introduces to the model fit is negligible. The Carreau parameters learned from flow-MRI vs. rheometry are shown in figure 5. We observe that the parameters learned from flow-MRI agree with rheometry data, considering uncertainties (table 5b), and that the learned effective viscosity field fits the rheometry data (figure 5a). As in the case of learning from flow-MRI, it is not possible to infer  $\mu_\infty$  and  $\lambda$  with high certainty when data,  $\mu_e(\dot{\gamma})$ , for  $\dot{\gamma} \gg 200 \text{ s}^{-1}$  are missing (rheometer flow instability onset).

## 5. Summary and conclusions

We have formulated a Bayesian inverse N-S problem that assimilates velocimetry data of 3D steady incompressible flow in order to jointly reconstruct the flow field and learn the unknown



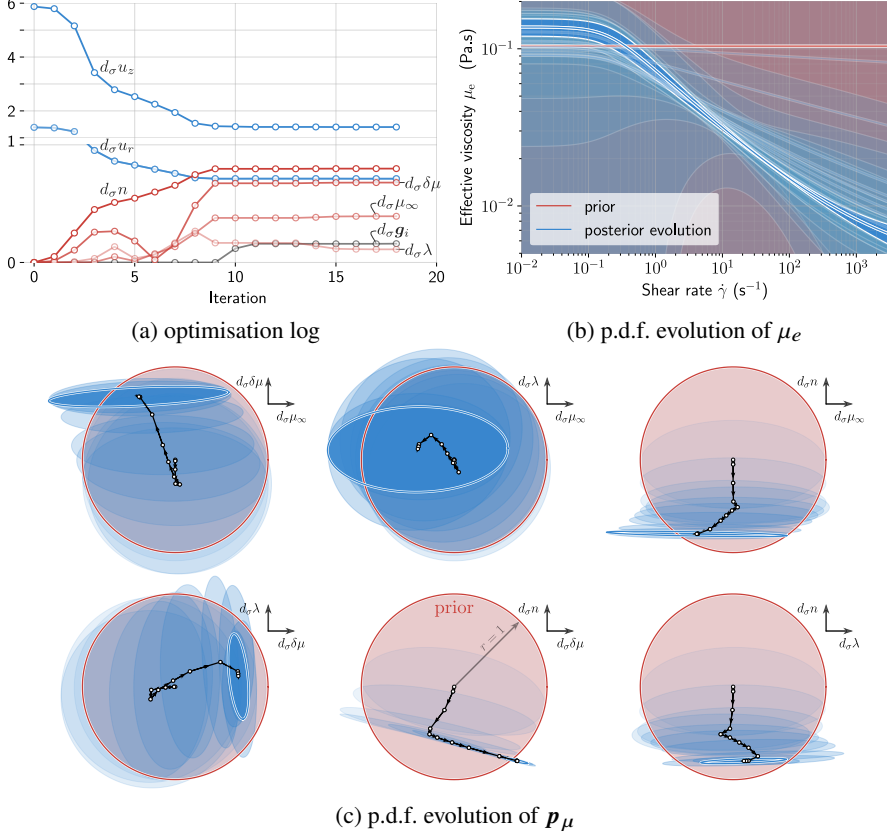


Figure 4: Optimisation log (figure 4a), and posterior p.d.f. evolution of the effective viscosity (figure 4b) and the Carreau parameters (figure 4c). In figure 4c the axes are such that  $d_{\sigma}x := (x - \bar{x})/\sigma_{\bar{x}}$ , where  $\bar{x}$  is the prior mean, and  $\sigma_{\bar{x}}$  is the prior standard deviation.

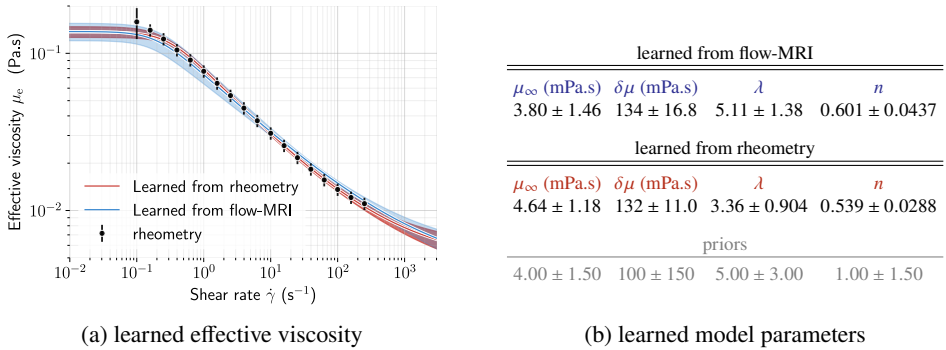


Figure 5: Learned Carreau fit to rheometry data, learned model parameters (MAP estimates), and assumed priors. Uncertainties in the figures correspond to  $3\sigma$  intervals.

N–S parameters. By incorporating a Carreau shear-thinning viscosity model into the N–S problem, we devise an algorithm that learns the Carreau parameters of a shear-thinning fluid, and estimates their uncertainties, from velocimetry data alone. Then we conduct a flow-MRI experiment to obtain velocimetry data of an axisymmetric laminar jet through an idealised medical device (FDA nozzle), for a blood analogue fluid. We show that the

algorithm successfully reconstructs the noisy flow field, and, at the same time, learns the Carreau parameters and their uncertainties. To ensure that the learned Carreau parameters explain the rheology of the fluid, instead of simply fitting the velocimetry data, we conduct an additional rheometry experiment. We find that the Carreau parameters learned from the flow-MRI data alone are in very good agreement with the parameters learned from the rheometry experiment (taking into account their uncertainties), and that the learned effective viscosity field fits the rheometry data. In this paper we have applied the algorithm to a Carreau fluid. The present algorithm, however, accepts any generalised Newtonian fluid, as long as the model is (weakly) differentiable. More complicated non-Newtonian behaviour, such as viscoelasticity, can be learned from velocimetry data if a viscoelastic model (e.g., Oldroyd-B fluid) is incorporated into the N–S problem.

## REFERENCES

- BROOKSHIER, K. A. & TARBELL, J. M. 1993 Evaluation of a transparent blood analog fluid: Aqueous Xanthan gum/glycerin. *Biorheology* **30**, 107–116, 2.
- ELKINS, C. J. & ALLEY, M. T. 2007 Magnetic resonance velocimetry: applications of magnetic resonance imaging in the measurement of fluid motion. *Experiments in Fluids* **43** (6), 823–858.
- GOLDFARB, D., REN, Y. & BAHAMOU, A. 2020 Practical Quasi-Newton Methods for Training Deep Neural Networks. In *Advances in Neural Information Processing Systems* (ed. H. Larochelle, M. Ranzato, R. Hadsell, M.F. Balcan & H. Lin), , vol. 33, pp. 2386–2396. Curran Associates, Inc.
- GUDBJARTSSON, H. & PATZ, S. 1995 The Rician Distribution of Noisy MRI Data. *Magnetic Resonance in Medicine* **34** (6), 910–914.
- HARIHARAN, P., GIARRA, M., REDDY, V., DAY, S. W., MANNING, K. B., DEUTSCH, S., STEWART, S. F. C., MYERS, M. R., BERMAN, M. R., BURGEEEN, G. W., PATERSON, E. G. & MALINAUSKAS, R. A. 2011 Multilaboratory Particle Image Velocimetry Analysis of the FDA Benchmark Nozzle Model to Support Validation of Computational Fluid Dynamics Simulations. *Journal of Biomechanical Engineering* **133** (4), 041002.
- K., SHWETANK, T., GERHARD, K., SUNIL, E., ASAD & R., KRISHNA 2022 Ultrasound velocity profiling technique for in-line rheological measurements: A prospective review. *Measurement* **205**, 112152.
- KONTOGIANNIS, A., ELGERSMA, S. V., SEDERMAN, A. J. & JUNIPER, M. P. 2022 Joint reconstruction and segmentation of noisy velocity images as an inverse Navier–Stokes problem. *Journal of Fluid Mechanics* **944**, A40.
- KONTOGIANNIS, A., ELGERSMA, S. V., SEDERMAN, A. J. & JUNIPER, M. P. 2024 Bayesian inverse Navier–Stokes problems: joint flow field reconstruction and parameter learning. *Submitted to Inverse Problems* .
- MAGALHÃES, S. DA C., FOLSTA, M., NORONHA, E. V. N., SCHEID, C. M. & CALÇADA, L. A. 2017 Study of continuous rheological measurements in drilling fluids. *Brazilian Journal of Chemical Engineering* **34** (3), 775–788.
- RANFTL, S., MÜLLER, T. S., WINDBERGER, U., BRENN, G. & VON DER LINDEN, W. 2023 A Bayesian approach to blood rheological uncertainties in aortic hemodynamics. *International Journal for Numerical Methods in Biomedical Engineering* **39**.
- SEQUEIRA, A. & JANELA, J. 2007 *An overview of some mathematical models of blood rheology*. Springer Netherlands.
- STEWART, SANDY F. C., PATERSON, ERIC G., BURGEEEN, GREG W., HARIHARAN, PRASANNA, GIARRA, MATTHEW, REDDY, VARUN, DAY, STEVEN W., MANNING, KEEFE B., DEUTSCH, STEVEN, BERMAN, MICHAEL R., MYERS, MATTHEW R. & MALINAUSKAS, RICHARD A. 2012 Assessment of CFD Performance in Simulations of an Idealized Medical Device: Results of FDA’s First Computational Interlaboratory Study. *Cardiovascular Engineering and Technology* **3** (2), 139–160.
- TARANTOLA, A. 2005 *Inverse Problem Theory and Methods for Model Parameter Estimation*. SIAM.
- WORTHEN, J., STADLER, G., PETRA, N., GURNIS, M. & GHATTAS, O. 2014 Towards adjoint-based inversion for rheological parameters in nonlinear viscous mantle flow. *Physics of the Earth and Planetary Interiors* **234**, 23–34.